Label-free assessment of adipose-derived stem cell differentiation using coherent anti-Stokes Raman scattering and multiphoton microscopy

Rabah Mouras
Pierre O. Bagnaninchi
Andrew R. Downes
Alistair P. D. Elfick

Label-free assessment of adipose-derived stem cell differentiation using coherent anti-Stokes Raman scattering and multiphoton microscopy

Rabah Mouras,[a] Pierre O. Bagnaninchi,[b] Andrew R. Downes,[a] and Alistair P. D. Elfick[a]
[a]University of Edinburgh, School of Engineering, Institute for Materials and Processes, King's Buildings, Mayfield Road, Edinburgh EH9 3JL, United Kingdom
[b]University of Edinburgh, MRC Centre for Regenerative Medicine, Edinburgh, EH16 4SB, United Kingdom

Abstract. Adult stem cells (SCs) hold great potential as likely candidates for disease therapy but also as sources of differentiated human cells *in vitro* models of disease. In both cases, the label-free assessment of SC differentiation state is highly desirable, either as a quality-control technology ensuring cells to be used clinically are of the desired lineage or to facilitate *in vitro* time-course studies of cell differentiation. We investigate the potential of nonlinear optical microscopy as a minimally invasive technology to monitor the differentiation of adipose-derived stem cells (ADSCs) into adipocytes and osteoblasts. The induction of ADSCs toward these two different cell lineages was monitored simultaneously using coherent anti-Stokes Raman scattering, two photon excitation fluorescence (TPEF), and second harmonic generation at different time points. Changes in the cell's morphology, together with the appearance of biochemical markers of cell maturity were observed, such as lipid droplet accumulation for adipo-induced cells and the formation of extra-cellular matrix for osteo-induced cells. In addition, TPEF of flavoproteins was identified as a proxy for changes in cell metabolism that occurred throughout ADSC differentiation toward both osteoblasts and adipocytes. These results indicate that multimodal microscopy has significant potential as an enabling technology for the label-free investigation of SC differentiation. © *2012 Society of Photo-Optical Instrumentation Engineers (SPIE).* [DOI: 10.1117/1.JBO.17.11.116011]

Keywords: nonlinear optical; multiphoton microscopy; coherent anti-Stokes Raman scattering; second harmonic generation; two photon excitation fluorescence; live cell imaging; time-course imaging; adult stem cells.

Paper 12172P received Mar. 12, 2012; revised manuscript received Sep. 27, 2012; accepted for publication Sep. 28, 2012; published online Nov. 1, 2012.

1 Introduction

Adipose-derived stem cells (ADSCs) are adherent adult stem cells (SCs) with similar properties to mesenchymal stem cells (MSCs).[1] They are relatively easily isolated from lipoaspirates and as such represent an autologous source of SCs for regenerative medicine. In addition to being likely candidates for cell therapy, adult SCs can be useful *in vitro* models of disease. In both these cases, label-free assessment of the differentiation state of SCs is desirable for a number of reasons; for example, in therapeutic use, SC lineage will require close scrutiny to ensure only the desire cell type is deployed or to facilitate time-course studies of cell differentiation. Likely applications of ADSCs are for diseases of the bone and cartilage, including reconstructive surgery through cell therapy or tissue engineering.

Generally, endpoint functional assays are performed to assess SC differentiation. Typically when ADSCs are induced *in vitro* toward the osteogenic and adipogenic lineages, alizarin red or oil red O (ORO) staining is used to assay the formation of mineralized matrix and lipid droplets (LDs), respectively. Earlier signs of differentiation can be tracked by flow cytometry, RNA assays,[2] or by immunohistochemical staining of specific markers of mature phenotypes (i.e., osteocalcin for osteoblasts and fatty acid binding protein 4 (FABP4), for adipocytes).

Endpoint functional assays are widely used in regenerative medicine research to assess the differentiated state and to assess the efficiency of differentiation. However, they are usually destructive and time-consuming and, as a result, are unsuitable for time-course studies of differentiation. More importantly, stem-cell-based therapies will require that the differentiation state of SCs be assessed prior to their transplantation to avoid any undesired effects. Nonperturbing and label-free assessments are desirable to preserve the therapeutic potential of the cells.

The identification of different molecular species at the microscopic scale is still a considerable challenge in many areas of the life sciences. Spontaneous Raman spectroscopy is a noninvasive technique, which probes a molecule's intrinsic vibrational modes. Detecting the vibrational signatures of molecules circumvents the need for fluorescent or other extrinsic markers and permits the visualization of the distribution of specific molecules (chemically selective imaging) with high sensitivity. Unfortunately, low signal levels limit the utility of this technique; either a large number of molecules or long acquisition times are required, precluding real-time imaging of living cells.

Coherent anti-Stokes Raman scattering (CARS) microscopy[3] is a four-wave mixing process in which molecular vibrations are driven coherently through stimulated excitation by pulsed lasers. Due to the nonlinear nature of the process, the signal is greatly amplified by around five orders of magnitude over traditional Raman spectroscopy. This significant signal increase offers new

Address all correspondence to: Rabah Mouras, University of Edinburgh, School of Engineering, Institute for Materials and Processes, King's Buildings, Mayfield Road, Edinburgh EH9 3JL, United Kingdom. Tel: +44 131 650 5696, Fax: +44 131 650 6551; E-mail: r.mouras@ed.ac.uk

possibilities of chemically selective imaging with high sensitivity and three-dimensional (3-D) sectioning.[4–9] CARS microscopy has the potential to make a significant contribution to biomedical imaging, offering new insights into biochemistry and pathways with sub-cellular spatial resolution.

Multiphoton microscopy, such as two photon excitation fluorescence (TPEF) and second harmonic generation (SHG), allows noninvasive and stain-free imaging of living cells and tissues using endogenous contrast. TPEF has been used to characterize cell viability, morphology, and proliferation in tissue. Recently, TPEF has enabled researchers to monitor the metabolic activity, morphology and oxidative stress of human MSCs[10–12] by imaging the autofluorescence of flavoproteins (FPs) and reduced nicotinamide adenine dinucleotide (NADH). It has been reported that FPs fluoresce when oxidized and do not when reduced. On the other hand, NADHs fluoresce when reduced and do not when oxidized, thus allowing redox state to be used to monitor the metabolism of the cells.[13,14] In addition, SHG generated by collagen content has been used to image extracellular collagen deposition[10] and to noninvasively quantify the collagen fiber content and organization in thick collagen gels.[15] Thus TPEF and SHG microscopy of ADSCs undergoing differentiation can be used as a direct method to characterize cell morphology and the deposition of fibrous collagen.

The combination of CARS microscopy with TPEF and SHG promises a wealth of chemical and biological information that could help to address some of the most persistent biological questions.[8] The multimodal imaging approach has great potential to contribute to drug delivery monitoring[9] and diagnosis of diseases like cancer,[16,17] atherosclerosis[18] and neurodegeneration.[19]

In this study, we investigate the noninvasive and label-free assessment of ADSCs during their differentiation toward osteoblast and adipocyte lineages by means of CARS, TPEF, and SHG.

2 Materials and Methods

2.1 Cell Culture

Human ADSC (Invetrogen, Ltd., Paisley, United Kingdom) were expanded to passage 3 in a low serum medium (complete RS MesenPRO, Invetrogen, Ltd., Paisley, United Kingdom) supplemented with 2 mM L-glutamine in accordance with the supplier's protocol. Cells were cultured in glass-bottom Petri dishes (Fluorodish Cell Culture Dish; 35 mm, World Precision Instruments, Invetrogen, Ltd., Paisley, United Kingdom) to an initial density of 5000 cells per cm^2 in a humidified incubator (37°C and 5% CO_2). As described previously,[20] at $t = 93$ h

ADSCs were induced toward osteoblastic or adipocytic lineages with an appropriate differentiation media (osteogenesis or adipogenesis media, Invitrogen). Two weeks post-induction, end-point staining was performed to confirm that ADSCs had been induced toward osteoblasts (Alizarin red) and adipocytes (ORO), as shown in Fig. 1.

2.2 Multimodal Microscopy

The experimental setup used in this study has been described elsewhere.[8] Briefly, a mode-locked Nd : YVO$_4$ laser source (Pico-Train, High-Q Laser, Hohenems, Austria) produces the Stokes pulse (7.5 ps, 1064.4 nm) and a 5 ps, frequency-doubled, 532-nm beam, which was used to pump a picosecond optical parametric oscillator (OPO) (Levante Emerald, APE, Berlin, Germany). The OPO delivers a signal tunable in the range 700 to 1000 nm that was used as a pump in the CARS process or to excite the TPEF and SHG. The two beams are combined in a collinear geometry and focused on the sample using a 60× oil immersion objective (Plan Apo VC 60×, NIKON, Amsterdam, Netherlands) with 1.4 numerical aperture (NA). A laser-scanning, confocal, inverted optical microscope (C1 Eclipse, Nikon BV, Amsterdam, Netherlands) is used to acquire images. Appropriate sets of custom short-pass (SP) and bandpass filters (Chroma, Rockingham, USA) are used to suppress the radiation at the laser wavelengths and selectively transmit the nonlinear optical (NLO) signals. The configuration of the system enables both backward (epi-) and forward detection schemes. The system also comprises a heating stage to maintain living cells at 37°C. A schematic diagram of our multimodal microscope is presented in Fig. 2.

2.2.1 CARS microscopy

For CARS measurements, the pump laser was tuned to 817 nm (12,240 cm^{-1}) where the frequency difference with the Stokes beam 1064.4 nm (9395 cm^{-1}) matches the CH$_2$ vibration at 2845 cm^{-1} of lipids, giving a CARS signal at 662.9 nm (15,085 cm^{-1}). SP filters (945SP, 775SP, and 700SP), and a bandpass filter (660/13, FWHM = 13 nm) were used to collect the CARS signal. The laser power at the sample was 12 mW and 8 mW for the pump and Stokes beams, respectively.

2.2.2 TPEF and SHG microscopy

Our multimodal microscope features a three-channel detection scheme. Thus, TPEF and SHG signals can be acquired
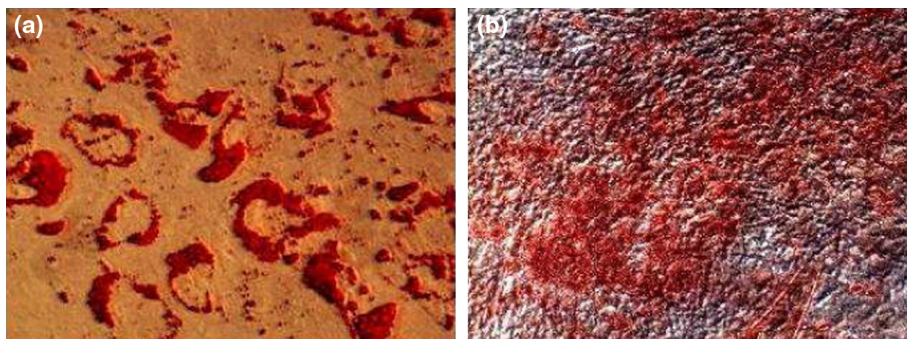
Fig. 1 Optical images of stained ADSC induced toward adipocyte and osteoblasts after 10 days post-induction. (a) Oil-red-O staining demonstrated mature lipid droplets accumulation in ADSCs induced toward adipocytes. (b) Alizarin red staining was positive for ADSCs induced toward osteoblasts showing the first signs of mineralization.
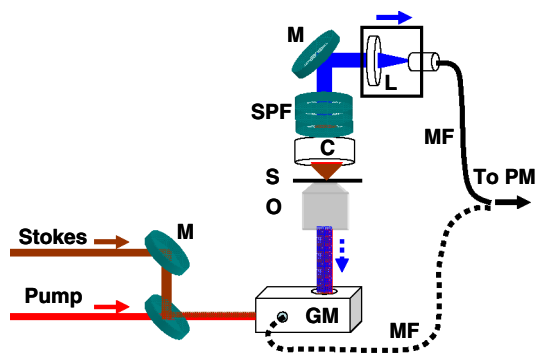
Fig. 2 Schematic diagram of Multimodal microscope setup: M = mirror; DM = dichroic mirror; GM = galvano mirrors; O = objective lens; S = sample; C = condenser lens; SPF = short pass filter set; L = focusing lens; MF = multimodal optical fiber; PM = photomultiplier.

simultaneously with a CARS signal. However, in our experiments we used only the forward direction to collect the NLO signals using a multimode optical fiber coupled to two photomultipliers. A dichroic mirror 570/LP (LP: long-pass) is used to separate the two signals while bandpass filters 609/54 and 414/46 were used to respectively acquire TPEF and SHG signals. The Stokes beam was blocked during SHG measurements.

2.3 Image Analysis: Quantitative Assessment of Fibrous Collagens and Lipid Droplets

Images of the differentiating cells were captured at 2, 5, 7, 10, and 14 days post-induction. To quantify collagen density from

SHG measurements we followed the procedure described in literature.[10,15] Briefly, SHG images were converted to 8-bit format, smoothed with a 3×3 averaging filter, and finally an automatic thresholding was performed to binarize the data using the image processing software Image J. The SHG pixel density may then be defined as the mean number of positive pixels calculated over several SHG images ($N = 4$) for time point the number of SHG positive pixels divided by the total number of pixels in the image. Similarly, to quantify the LDs accumulation, CARS images were thresholded with a similar protocol, and LDs mean pixel density was defined as the number of positive pixels over the total number of pixels.

Finally, one-way analysis of variance (ANOVA) tests were performed to determine whether one group was significantly different from the others, followed by a Tukey–Kramer multi-comparison test to determine which groups were significantly different. The level of statistical significance was set to $p < 0.05$. Likewise, the mean LDs density may be defined following the same protocol on CARS images ($N = 3$).

3 Results

3.1 ADSCs Induced Toward Adipocytes

ADSCs induced toward adipocytes are characterized by the presence of intracellular LDs mainly around the nuclei. To monitor the differentiation of ADSC cells to adipocytes, CARS and TPEF images of living cells were taken at different stages of differentiation. Images obtained after 2, 7, and 10 days post-induction are presented in Fig. 3. Two days after induction, the CARS image shows many small bright spots corresponding
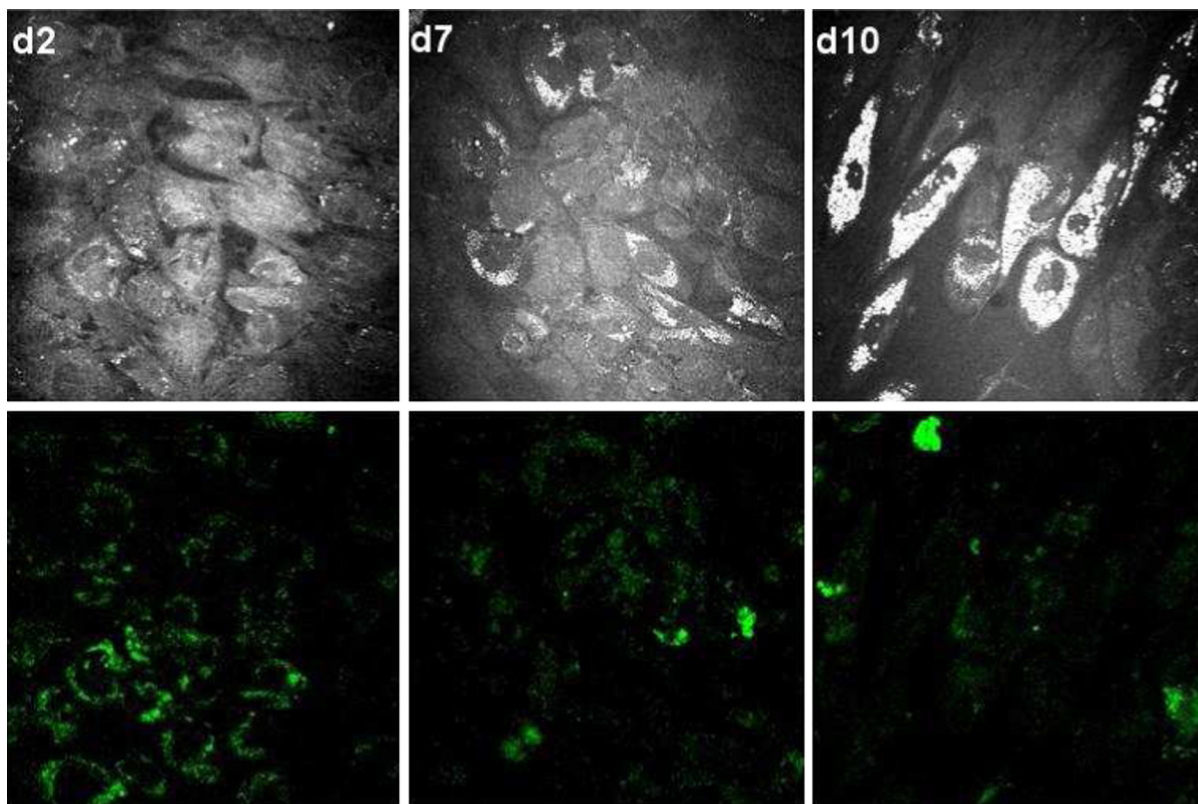
Fig. 3 Multimodal images of ADSC cells induced toward adipocytes at different stages post-induction: (2, 7, and 10 days). Top row: CARS images of the CH_2 stretch frequency, which is dominated by lipids at 2845 cm^{-1}. Bottom row: TPEF of FPs acquired using a band-pass filter at 609 nm. Image size $212 \times 212 \ \mu m^2$, and the acquisition time is 21 s for all images.
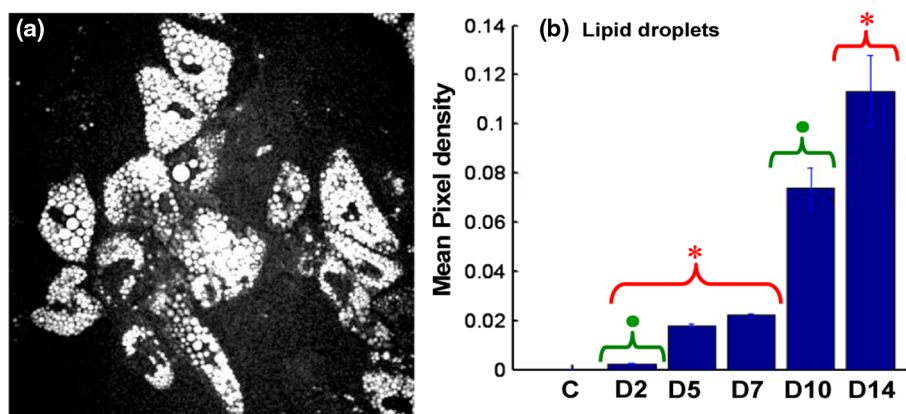
Fig. 4 (a) CARS image of the CH_2 stretch frequency which is dominated by lipids at 2845 cm^{-1} showing the lipid droplets surrounding the nuclei in adipo-induced cells at day 14 day post-induction. Image size is 212 × 212 μm^2 and the acquisition time was 1 s. (b) Quantitative evaluation of lipid droplets production. CARS pixel density from adipo-genic cells was significantly increased at each time point showing the augmentation of lipid contents of adipo-induced cells in time (compared to the previous day). No collagen deposition was observed in the adipo-induced cells. $N = 3$. Statistical differences in mean values compared to the previous time point are indicated by an asterisk or a closed circle. (C is the control sample before induction.)

to LDs near the periphery of the nuclei in adipo-induced cells (Fig. 3-d2). Moreover, a change of morphology to a more rounded shape and an apparent increase in the mean cell diameter are observed for cells undergoing adipogenesis in good agreement with literature.[21] Figure (3-d7 and 3-d10) show further accumulation of LDs. These changes were accompanied by an increase in TPEF suggesting an increased metabolic activity of the cells starting to differentiate to adipocytes. At d7, the LDs became larger and well structured around the nuclei, their size appearing to increase continuously until they completely fill the cytoplasm surrounding the nuclei after 10 days. These changes are accompanied by a decrease in the TPEF signal, which may indicate a change in the differentiation process. LD accumulation was confirmed by ORO staining as shown in Fig. 1. The evolution of LDs for each time point of differentiation is depicted in Fig. 4(b). Mean LDs pixel density increased at each time point showing the augmentation of lipid contents of adipo-induced cells. By d10, statistically significant differences in LDs accumulation were observed from control and d2. These differences are even more noticeable by d14 [Fig. 4(a)]. D14 was found significantly different from d7, d5, and d2 ($p < 0.05$) as indicated in Fig. 4(b).

3.2 ADSC Induced Toward Osteoblasts

Osteo-induced cells are characterized mainly by changes in morphology, the formation of an extracellular matrix of collagen[22] and hydroxyapatite (HA) mineralization.[23] To monitor the differentiation of ADSCs toward osteoblasts, we acquired multimodal images at different time points. Representative CARS, TPEF, and SHG images are presented in Fig. 5.

CARS images of the cells obtained at 2845 cm^{-1} demonstrated that two days after induction, the cells became more elongated than ADSCs, in accordance with data reported previously.[21] They covered the substrate more effectively when compared to adipo-induced cells. These morphological changes were accompanied by the appearance of fluorescent features surrounding the nuclei. This autofluorescence may be attributed to oxidized FPs.[10] At this early stage of differentiation, no signs of collagen formation were observed.

At d7 post-induction, collagen fibers were observed together with an increase of fluorescent structures surrounding the nuclei (Fig. 5-d7). At d10, autofluorescence of FPs became even stronger and colocalized with areas where the collagen matrix was denser (Fig. 5-d10). Quantitative analysis of SHG images indicates the gradual deposition of fibrous collagens by cells undergoing differentiation toward osteoblasts. Mean values of SHG pixel density clearly increased over time [Fig. 6(b)]. By d10, statistically significant differences in collagen fibers deposition were observed from previous data points and became even more evident by d14 [Fig. 6(a)]. D14 and d10 were found significantly different from d7, d5, and d2 ($p < 0.05$) as indicated in Fig. 6(b).

In order to follow the morphological changes of ADSCs during the differentiation process towards osteoblasts, we acquired 3-D multimodal images. CARS images show that cells undergoing osteogenesis were growing in multiple layers (Fig. 7). Eventually some cells were found with a rounded shape approaching the shape of bone cells (dashed circles). At this stage we expect the appearance of the first signs of mineralization. Typically, the formation of minerals starts between the 10th and 15th day post-induction, as confirmed by Alizarin red staining used to validate the osteoblast lineages (Fig. 1).

4 Discussion

Nonlinear multimodal imaging has been demonstrated as a label-free technique to observe early signs of adipocyte differentiation. Accumulated LDs are densely structured and, as a consequence, exhibited a strong CARS signal, facilitating their early detection. Moreover, their formation is observed to be preceded by a strong TPEF signal that could correlate with a high metabolic activity. This autofluorescence emanated from small structures surrounding the nuclei and can be attributed to oxidized FPs. This is in good agreement with literature suggesting an increase in the redox state of the SC (ratio of reduced NADH to FPs) upon transition from multipotent to differentiated state.[10–12]

TPEF images showed an increase in fluorescence until the midstage and then a decrease until the late stage of differentiation, at which point cells undergoing adipogenesis showed less fluorescence, indicating less activity. Moreover, at late time
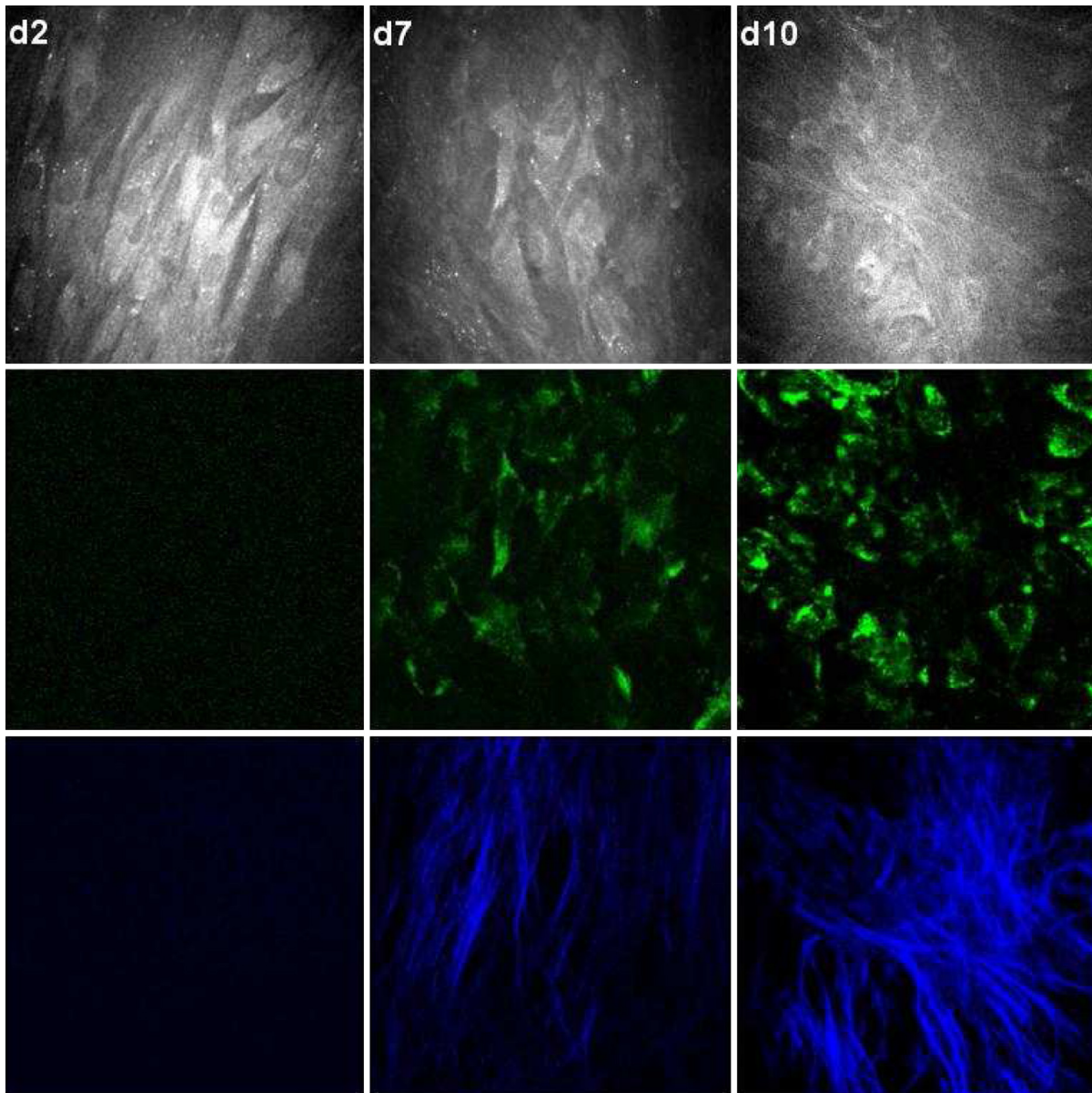
Fig. 5 Multimodal images of ADSC cells induced towards osteoblasts at different stages post-induction: (2, 7, and 10 days). Top row: CARS images of the CH_2 stretch frequency which is dominated by lipids at 2845 cm^{-1}. Middle row: TPEF of FPs, acquired using a band-pass filter at 609 nm. Bottom row: SHG of collagen fibers acquired using a band-pass filter at 414 nm. Image size 212 × 212 μm^2 and the acquisition time was 21 s for all images.

points, some cells did not show any fluorescence, possibly indicating non-differentiating cells.

Quantitative analysis of CARS pixel density allowed the identification of two groups with significant statistical differences ($p < 0.05$). D14 is significantly different from d7, d5, and d2, while d10 is only different from d2 and C [Fig. 4(b)]. These data show that the earliest time point at which significant differences occur is d10 post-induction. LD accumulation was clearly observable in few cells at d7 (see Fig. 3) and d5 (data not shown), but the scarcity of LD rich cells created too much variance over the number of pictures per day to achieve statistical significance.

The same investigation was carried out on ADSCs induced toward osteoblasts. At an early stage (two days post-induction) a clear change in cell morphology was observed, accompanied by the formation of fluorescent structures near the periphery of the nuclei. This fluorescence is less pronounced when compared with that observed in cells undergoing adipogenesis (Fig. 5-d2). This may signify that the osteo-induced cells are less metabolically active. The fluorescence was found to increase over the period of the experiment and to be localized to small structures around the nuclei. Correspondingly high metabolic activity was accompanied by the formation of collagen fibers as shown in the SHG image (Fig. 5-d7). The co-location of TPEF and SHG suggests that the deposition of collagen originated from the highly active cells. At a late stage of differentiation, the collagen matrix becomes denser, while the TPEF signal increases continuously (Fig. 5-d10). Quantitative evaluation of SHG pixel density [Fig. 6(b)] demonstrated that collagen fiber content significantly increased over time, indicating that collagen production may start even before d5. From d10 substantial increases in collagen content are observed, in good correlation
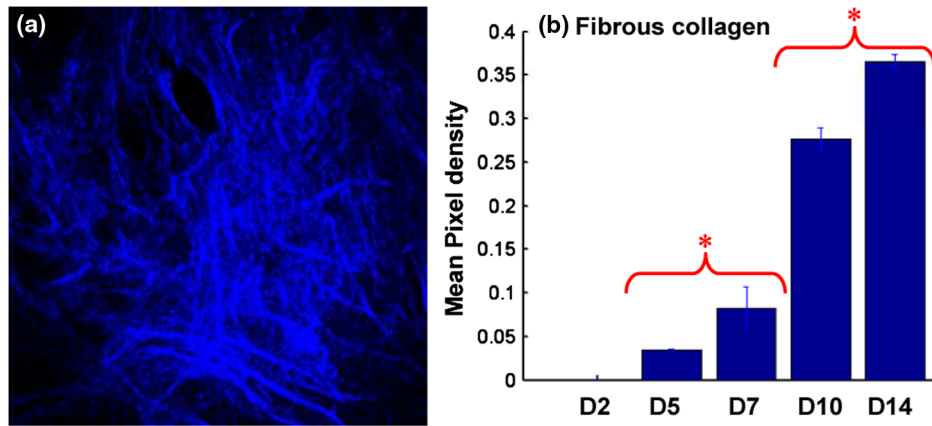
Fig. 6 (a) SHG image of fibrous collagen in osteo-induced cells at day 14 post-induction. Image size is $212 \times 212 \ \mu m^2$ and the acquisition time was 21 s. (b) Quantitative evaluation of fibrous collagen formation. The gradual deposition of fibrous collagens is apparent in SHG images acquired on days 5, 7, 10, and 14. Quantitative evaluation of pixel density in SHG images was significantly increased at each time point (compared to the previous day) revealing that collagen production may start before day 5. $N = 4$. Statistical differences in mean values compared to the previous time point are indicated by an asterisk.
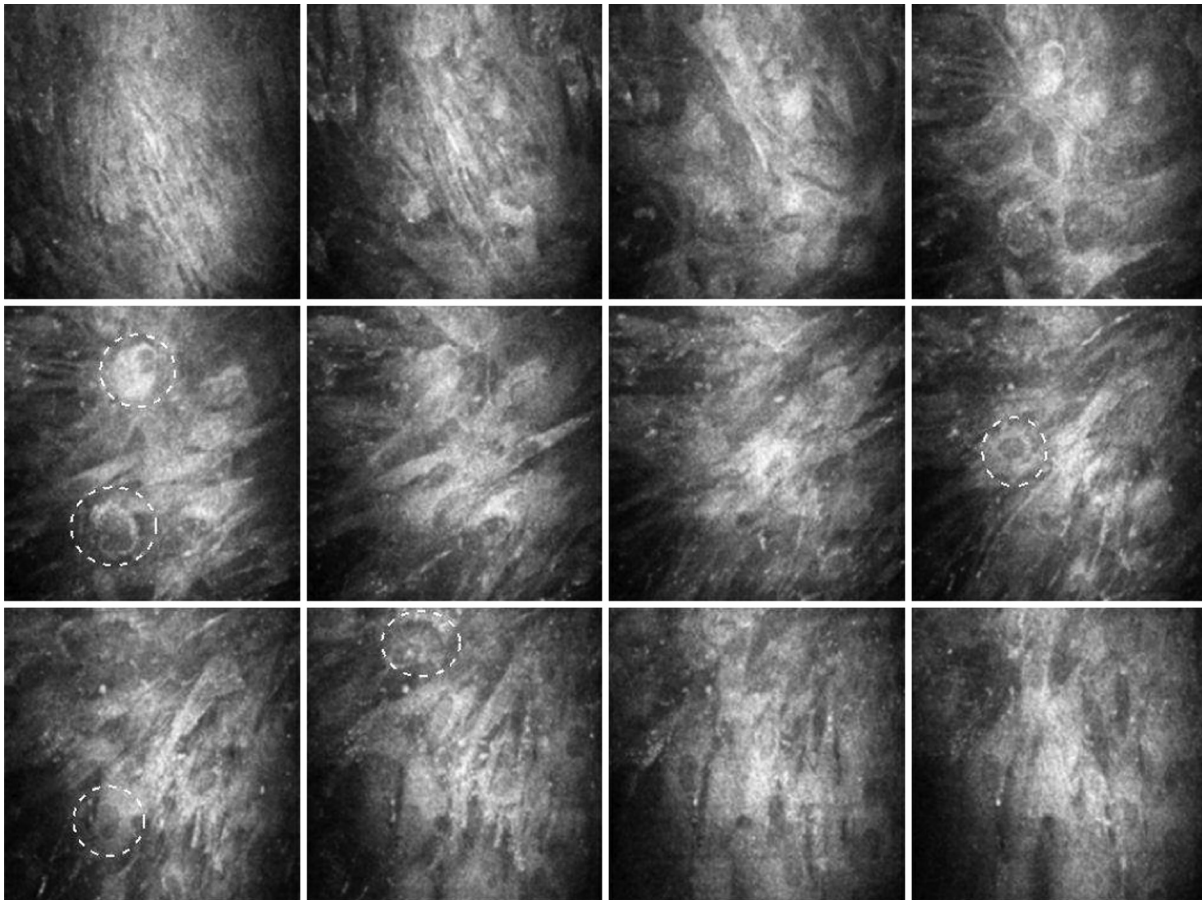
Fig. 7 Z-stack of 12 CARS images of the CH_2 stretch frequency, which is dominated by lipids at 2845 cm^{-1} of ADSCs differentiated toward osteoblasts at day 10 post-induction taken with 1 μm steps from the bottom (top left image). Pictures show a multilayered distribution of the cells. Note the different morphologies of the cells. Larger cells, closer to the real morphology of bone cells, can be observed (dashed circles). Image size $212 \times 212 \ \mu m^2$ and the acquisition time is 21 s for all images.

with Fig. 5, showing that collagen fibers become denser and thicker at mid- and late-stages of differentiation.

When comparing Figs. 3 and 5, it is clear that CARS imaging has the ability to distinguish changes in cell phenotype as early as two days post-induction. Comparison with phase contrast microscopy images showed CARS very capable of resolving cell morphology, with nuclei apparent by signal contrast. It is probable that image processing, together with automated scanning, could enable the screening of SC-based *in vitro* models. It is worth noting that the efficiency of differentiation could be calculated from these images as the ratio of differentiated cells to undifferentiated cells, providing that larger areas are

scanned. The potential deployment of SC-based therapies would require that researchers develop novel growth media (free from animal-based products and chemically well-defined) and substrates for expansion and differentiation of SCs in culture. As a consequence, quantitative methods of stem-cell maintenance and differentiation are increasingly important. In our study CARS imaging was conducted on the same sample over a period of 15 days with no adverse effects, a clear demonstration of its nonperturbing nature.

Figure 7 exemplifies a further advantage of CARS microscopy over transmission light or phase contrast images: 3-D CARS images reveal multilayered growth of the cells induced toward osteogenesis, as well as the presence of rounded cells approaching the morphology of primary bone cells (dashed circles in Fig. 7). Such information cannot be extracted from conventional light transmission or phase contrast images. We can anticipate that these cells were maturing to osteoblasts. These findings were confirmed by means of Alizarin red staining (Fig. 1).

Finally, it is worth noting that there exists the possibility to quantify HA mineralization, which would significantly enhance the usefulness of CARS microscopy for assessing SC differentiation toward osteoblasts. A recent Raman study from this group showed the appearance of Raman peaks corresponding to mineralization; associated with phosphate (in hydroxyapatite) and carbonate.[24] Thus CARS imaging can potentially be conducted with excitation tuned to the characteristic Raman peak relating to HA, which is produced in the extracellular matrix, and carbonate, observed at 960 cm^{-1} and 1067 cm^{-1}, respectively.[25] We can similarly anticipate that nuclear imaging with CARS at the wave number associated with DNA backbone (1095 cm^{-1})[26] could in the future be performed to facilitate cell counting and the assessment of the efficiency of differentiation as the ratio of differentiated cells over undifferentiated ones. The anti-Stokes wavelengths corresponding to these frequencies are 863.6 nm (DNA), 867.4 nm (HA), and 883.8 nm (carbonate). At these low wave numbers, the nonresonant background (NRB) represents a major challenge to CARS microscopy; however, it has been demonstrated that it is still possible to image at these wave numbers using high laser powers and long acquisition times.[24,27,28] To become an attractive technology, more development is required to minimize the potential for photodamage encountered through this need to apply very high laser powers or long time acquisitions. This includes the employment of more sensitive detectors to wavelengths above 800 nm, removal of NRB using frequency modulated CARS,[29] polarization CARS,[30] heterodyne polarization CARS,[31] etc. or implementing alternative techniques such as stimulated Raman scattering (SRS) microscopy.[32]

5 Conclusion

The induction of ADSCs toward two different cell lineages was monitored in parallel using CARS, TPEF, and SHG microscopy. Multimodal imaging shows the potential to track and quantify differentiation state with the same efficiency as normal confocal fluorescence microscopy but without the need to employ labeling agents. Multiphoton microscopy holds considerable promise for the negligibly invasive assessment of the differentiation state of SCs, opening the prospect of its use to assess cells for therapeutic deployment in regenerative medicine.

References

1. P. Zuk et al., "Human adipose tissue is a source of multipotent stem cells," *Mol. Biol. Cell* **13**(12), 4279–4295 (2002).
2. H. Fukuda et al., "Fluorescence-activated cell sorting–based purification of embryonic stem cell–derived neural precursors averts tumor formation after transplantation," *Stem Cells* **24**(3), 763–771 (2006).
3. A. Zumbusch, G. Holtom, and X. S. Xie, "Three-dimensional vibrational imaging by coherent anti-Stokes Raman scattering," *Phys. Rev. Lett.* **82**(20), 4142–4145 (1999).
4. M. Müller and J. Schins, "Imaging the thermodynamic state of lipid membranes with multiplex CARS microscopy," *J. Phys. Chem. B* **106**(14), 3715–3723 (2002).
5. A. Kachynski et al., "Realignment-enhanced coherent anti-Stokes Raman scattering and three-dimensional imaging in anisotropic fluids," *Opt. Express* **16**(14), 10617–10632 (2008).
6. C. L. Evans and X. S. Xie, "Coherent anti-Stokes Raman scattering microscopy: chemically selective imaging for biology and medicine," *Annu. Rev. Anal. Chem.* **1**(1), 883–909 (2008).
7. M. Müller and A. Zumbusch, "Coherent anti-Stokes Raman scattering microscopy," *Chem. Phys. Chem.* **8**(15), 2156–2170 (2007).
8. R. Mouras et al., "A multi-modal, multi-photon microscope for biological imaging," *Proc. SPIE* **7569**, 756933 (2010).
9. R. Mouras et al., "Nonlinear optical microscopy for drug delivery monitoring and cancer tissue imaging," *J. Raman Spectrosc.* **41**(8), 848–852 (2010).
10. W. L. Rice, D. L. Kaplan, and I. Georgakoudi, "Two-photon microscopy for non-invasive, quantitative monitoring of stem cell differentiation," *PLoS ONE* **5**(4), e10075 (2010).
11. W. L. Rice, D. L. Kaplan, and I. Georgakoudi, "Quantitative biomarkers of stem cell differentiation based on intrinsic two-photon excited fluorescence," *J. Biomed. Opt.* **12**(6), 060504 (2007).
12. J. M. G. Reyes et al., "Metabolic changes in mesenchymal stem cells in osteogenic medium measured by autofluorescence spectroscopy," *Stem Cells* **24**(5), 1213–1217 (2006).
13. B. Chance et al., "Intracellular oxidation-reduction states *in vivo*," *Science* **137**(3529), 499–508 (1962).
14. M. R. Duchen, "Ca2+-dependent changes in the mitochondrial energetics in single dissociated mouse sensory neurons," *Biochem. J.* **283**(Pt 1), 41–50 (1992).
15. C. Bayan et al., "Fully automated, quantitative, noninvasive assessment of collagen fiber content and organization in thick collagen gels," *J. Appl. Phys.* **105**(10), 102042 (2009).
16. C. Krafft et al., "A comparative Raman and CARS imaging study of colon tissue," *J. Biophoton.* **2**(5), 303–312 (2009).
17. H-W. Wang et al., "Imaging and quantitative analysis of atherosclerotic lesions by cars-based multimodal nonlinear optical microscopy," *Arterioscler. Thromb. Vasc. Biol.* **29**(9), 1342–1348 (2009).
18. H-W. Wang, L. L. Thuc, and J-X. Cheng, "Label-free imaging of arterial cells and extracellular matrix using a multimodal CARS microscope," *Opt. Comm.* **281**(7), 1813–1822 (2008).
19. Y. Fu et al., "Coherent anti-Stokes Raman scattering imaging of myelin degradation reveals a calcium-dependent pathway in lyso-PtdCho-induced demyelination," *J. Neurosci. Res.* **85**(13), 2871–2881 (2007).
20. P. O. Bagnaninchi and N. Drummond, "Real-time label-free monitoring of adipose-derived stem cell differentiation with electric cell-substrate impedance sensing," *Proc. Natl. Acad. Sci. U. S. A.* **108**(16), 6462–6467 (2011).
21. P. A. Zuk et al., "Human adipose tissue is a source of multipotent stem cells," *Mol. Biol. Cell* **13**(12), 4279–4295 (2002).
22. S. Stewart et al., "Trends in early mineralization of murine calvarial osteoblastic cultures: a Raman microscopic study," *J. Raman Spectrosc.* **33**(7), 536–543 (2002).

23. L. L. McManus et al., "Raman spectroscopic monitoring of the osteogenic differentiation of human mesenchymal stem cells," *Analyst* **136**(12), 2471–2481 (2011).

24. A. Downes et al., "Raman spectroscopy and CARS microscopy of stem cells and their derivatives," *J. Raman Spectrosc.* **42**(10) 1864–1870 (2011).

25. H. K. Chiang et al., "*In situ* Raman spectroscopic monitoring of hydroxyapatite as human mesenchymal stem cells differentiate into osteoblasts," *J. Raman Spectrosc.* **40**(5), 546–549 (2009).

26. I. Notingher et al., "*In situ* spectral monitoring of mRNA translation in embryonic stem cells during differentiation *in vitro*," *Anal. Chem.* **76**(11), 3185–3193 (2004).

27. J-X. Cheng et al., "Laser-scanning coherent anti-Stokes Raman scattering microscopy and applications to cell biology," *Biophy. J.* **83**(1), 502–509 (2002).

28. S. O. Konorov et al., "*In situ* analysis of living embryonic stem cells by coherent anti-Stokes Raman microscopy," *Anal. Chem.* **79**(18), 7221–7225 (2007).

29. F. Ganikhanov et al., "High-sensitivity vibrational imaging with frequency modulation coherent anti-Stokes Raman scattering (FM CARS) microscopy," *Opt. Lett.*, **31**(12), 1872–1874 (2006).

30. F. Lu, W. Zheng, and Z. Huanga, "Heterodyne polarization coherent anti-Stokes Raman scattering microscopy," *App. Phys. Lett.* **92**(12), 123901 (2008).

31. J. X. Cheng, L. D. Book, and X. S. Xie, "Polarization coherent anti-Stokes Raman scattering microscopy," *Opt. Lett.* **26**(17), 1341–1343 (2001).

32. C. Freudiger et al., "Label-free biomedical imaging with high sensitivity by stimulated Raman scattering microscopy," *Science* **322**(5909), 1857–1861 (2008).